iScience

CellPress
OPEN ACCESS

Article

Dielectric behavior of curcuminoid polymorphs on different substrates by direct soft vacuum deposition

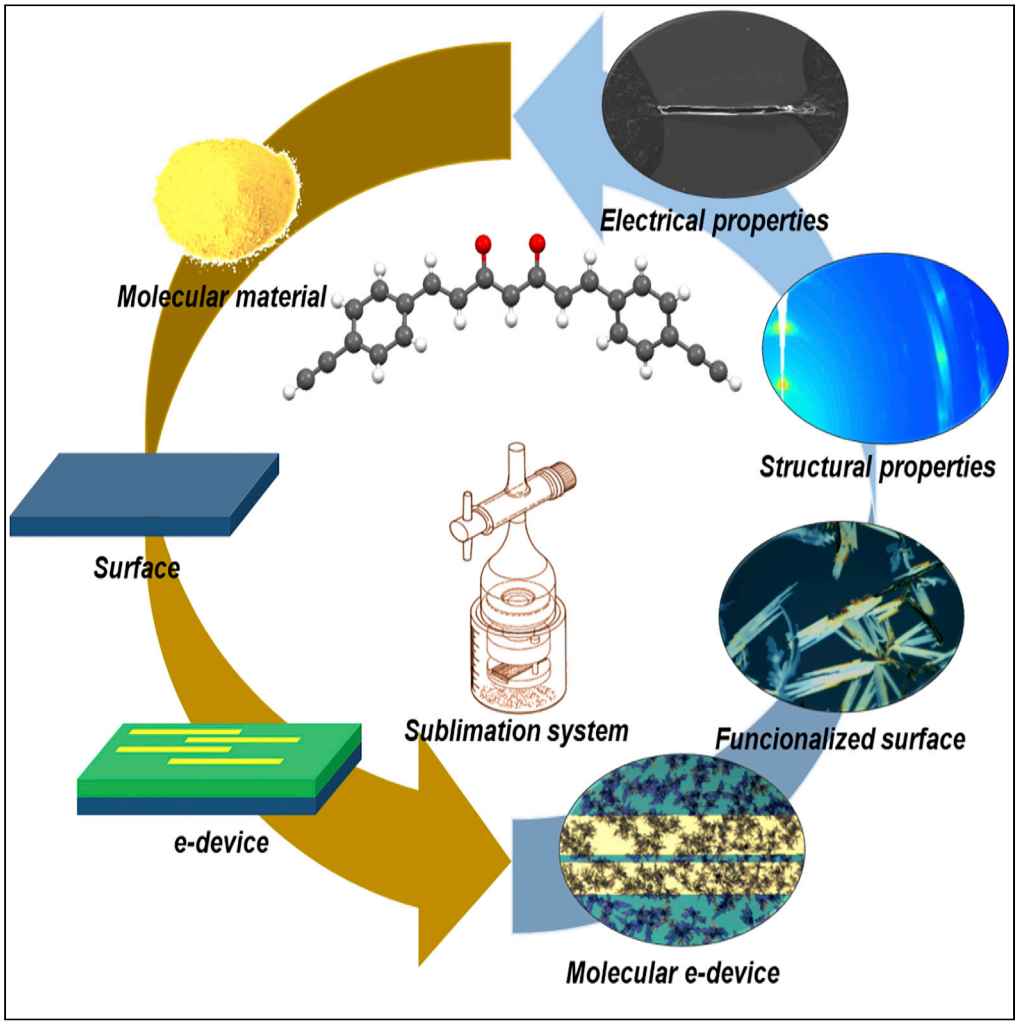

Daniel Riba-López, Rossella Zaffino, Daniel Herrera, ..., Eliseo Ruiz, Arántzazu González-Campo, Núria Aliaga-Alcalde

rpfattner@icmab.es (R.P.)
agonzalez@icmab.es (A.G.-C.)
nuria.aliaga@icrea.cat (N.A.-A.)

Highlights

A new curcuminoid with triple bonds ending groups shows dielectric behavior

Direct sublimation of the curcuminoid on substrates is achieved under mild conditions

Structural-electronic correlation on surfaces is a strong analytical tool

Permittivity is greatly affected by polymorphism

Riba-López et al., iScience 25, 105686
December 22, 2022
https://doi.org/10.1016/j.isci.2022.105686

iScience

CellPress
OPEN ACCESS

Article

Dielectric behavior of curcuminoid polymorphs on different substrates by direct soft vacuum deposition

Daniel Riba-López,[1,7] Rossella Zaffino,[1,7] Daniel Herrera,[1] Roc Matheu,[2,3] Francesco Silvestri,[1] Jesse Ferreira da Silva,[1,4] Eva Carolina Sañudo,[3,5] Marta Mas-Torrent,[1] Esther Barrena,[1] Raphael Pfattner,[1,*] Eliseo Ruiz,[2,3] Arántzazu González-Campo,[1,*] and Núria Aliaga-Alcalde[1,6,8,*]

SUMMARY

Our work examines the structural-electronic correlation of a new curcuminoid, AlkCCMoid, as a dielectric material on different substrates. For this purpose, we show a homemade sublimation method that allows the direct deposition of molecules on any type of matrix. The electronic properties of AlkCCMoid have been evaluated by measurements on single crystals, microcrystalline powder, and sublimated samples, respectively. GIWAXS studies on surfaces and XRD studies on powder have revealed the existence of polymorphs and the effect that substrates have on curcuminoid organization. We describe the dielectric nature of our system and identify how different polymorphs can affect electronic parameters such as permittivity, all corroborated by DFT calculations.

INTRODUCTION

The practical use of molecules as active components in electronic devices depends on the intrinsic electronic properties of the molecular system under study and their assembly in the solid state. For realistic applications, the substrate on which the molecules are deposited plays an important role as it influences molecular growth and ordering. As a result, new polymorphic forms can develop, which are often not observed in bulk single-crystals.[1–4] To ensure robust and efficient molecular elements, regardless of their electronic behavior, it is necessary to understand the impact that the assembly and substrate have on the parameters governing their final electronic properties.[5–7] This is in line with the study of new materials, analyzing in detail their structure-properties correlation, and the use of simple methods for their manipulation, with the aim of identifying and redesigning low-cost, environmentally friendly and high-performance molecular systems at the nano- and micro-scale.[8]

Curcuminoids (CCMoids) are a family of molecules extensively studied in the field of biomedicine, the best known of which is curcumin.[9] A large number of such systems and simple methodologies for their synthesis are now available,[10,11] together with reports on their physicochemical properties.[12–17] The versatility in their design is remarkable, functioning as molecular platforms, where variations in the different parts (central skeleton, diketone moiety, and aromatic groups, Figure 1A top) give rise to new structural compositions, with modified biological, optical and electronic behavior.[18] These diarylheptanoid systems are dyes, readily coordinate with transition metals and metalloids,[19,20] and often exhibit solvatochromic properties.[21] This has led to an expansion of the use of CCMoids in other areas of nanoscience and nanotechnology, attracting attention as key components in coordination polymers (CPs),[22] MOFs[17,23] and photovoltaic cells,[24,25] among others. In relation to the field of molecular electronics, CCMoids have been studied mainly in solution, showing band gap values of the order of 2-3 eV,[13,26] tuned through the coordination of the β-diketone group and the nature of the aromatic sides. As far as electronic devices are concerned, there are only a few examples reported with curcumin and coordinated systems, listed as appealing for ecofriendly applications in the framework beyond-CMOS devices,[27] although it is important to note that there has been increasing interest in boron difluoride CCMoids due to their potential optoelectronic applications.[28–30] Taking into account CCMoids structural diversity, their projection in molecular-based electronics is promising, but still limited,[27–36] with an increasing need to gather information and improve designs. Beyond their use as an active layer in electronic devices, wide band gap materials can be of interest as a dielectric in capacitors and transistors combined with different electronic elements.[37] In

[1]Institut de Ciència de Materials de Barcelona (ICMAB-CSIC) Campus Universitari, 08193 Bellaterra, Spain

[2]Institut de Recerca de Química Teòrica i Computacional, Universitat de Barcelona, Diagonal 645, 08028 Barcelona Spain

[3]Departament de Química Inorgànica i Orgànica, Universitat de Barcelona, C/Martí i Franqués 1-11, 08028 Barcelona, Spain

[4]University of Southampton, Chemistry, Highfield, Southampton, UK

[5]Institut de Nanociència i Nanotecnologia. Universitat de Barcelona, Av. Diagonal 645, 08028 Barcelona, Spain

[6]ICREA (Institució Catalana de Recerca i Estudis Avançats) Passeig Lluïs Companys 23, 08010 Barcelona, Spain

[7]These authors contributed equally

[8]Lead contact

*Correspondence: rpfattner@icmab.es (R.P.), agonzalez@icmab.es (A.G.-C.), nuria.aliaga@icrea.cat (N.A.-A.)

https://doi.org/10.1016/j.isci.2022.105686

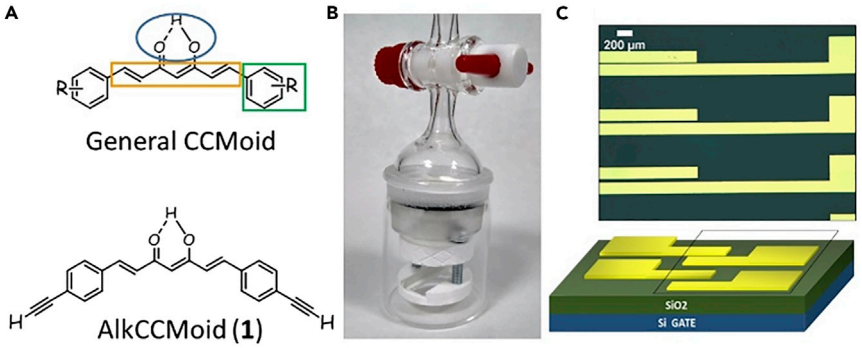

Figure 1. Illustration of molecules, sublimation system, and FET device

(A) Top. ChemDraw scheme of a general symmetric CCMoid (highlighting the β-diketone group, CCMoid skeleton, and aromatic groups in blue, orange, and green, respectively). Bottom. ChemDraw scheme of AlkCCMoid (1).

(B) Picture of the custom-designed sublimation system used in this work.

(C) Pictures of three-terminal devices on Si/SiO_2 substrate containing source and drain electrodes made of Au.

this regard, stable films of organic molecules with insulating properties, which can be easily deposited on a substrate by sublimation, could provide an environmentally sustainable alternative to standard oxides and insulators used in the manufacture of metal-insulator-semiconductor (MIS) and metal-oxide-semiconductor (MOS) devices. Some of us have performed single-molecule electronic transport studies using CCMoids as nanowires, by electrical controlled break junction (BJ) and mechanically controlled break junction (MCBJ) techniques, with conductance values on the order of other small, conjugated molecules; some CCMoids have been studied at room temperature in hybrid graphene devices and in other cases the critical factors for them to show electric-field induced bistability have been identified.[31–35]

Here we show a new synthetic CCMoid, the AlkCCMoid (1, Figure 1A bottom), highlighting its electrochemical and crystalline properties, focusing on its deposition studies. To avoid solvent interference, we exploited its ability to sublimate crystallizing on different surfaces and identify the conditions under which the system polymerizes. For that, we developed a homemade setup (patent pending, Figure 1B) which presents the advantage of carrying the sublimation directly on surfaces, under mild conditions (STAR Methods). The electrical performance of 1 was examined using microcrystalline powder (1-MP), single crystals (1-SC) and, sublimated material (1-SUB) on three-terminal devices containing Si/SiO_2/Au electrodes (Figure 1C) and related substrates (Au and Si/SiO_2). The analyses of the different crystalline phases were performed using powder XRD (X-ray Diffraction) and GIWAXS (Grazing Incidence Wide Angle X-ray Scattering) techniques. Focusing on the Si/SiO_2 substrates, we compared the diffraction patterns of 1 and evaluated supramolecular changes caused by temperature and sublimation, with the help of DFT calculations, identifying variations in the permittivity of the microcrystalline powder.

RESULTS AND DISCUSSION

AlkCCMoid (1) was synthesized, as a microcrystalline powder (1-MP), following a modification of the Pabonś method[10] according to the procedure shown in Scheme in STAR Methods, using MeCN as precipitating solvent. The experimental section is reported in detail in the SI. 1-MP was analyzed in solution by $^{1}H/^{13}C$ NMR (Figures S1 and S2) and additional techniques (UV-Vis absorption, IR, MALDI, and EA, Figures S5, S6, and S8), showing the expected CCMoid features. The optical band gap of 1-MP was assessed by solid UV-Vis absorption spectroscopy (KBr pellets, Figures S10 and S11, due to the already known solvatochromic behavior of CCMoids)[36,38–41] and the electrochemical energy gap, using CV (cyclic voltammetry, Figure S12).[42] Both measurements display an approximated value of 2.4 eV, corresponding to a behavior close to the boundary of a semiconductor/insulator material.[43] Table S1 shows a summary of the data.

Single crystals of AlkCCMoid (1-SC) were obtained by slow diffusion by dissolving 1-MP in an EtOAc/Hexanes mixture and used to determine the structure by single crystal X-ray diffraction.[15,19,36] 1-SC crystallizes in the monoclinic space group *Cc*. Figure 2A shows its structure and packing characteristics with the most significant crystallographic parameters listed in Table S2. Within the molecule, the C=O/C-OH

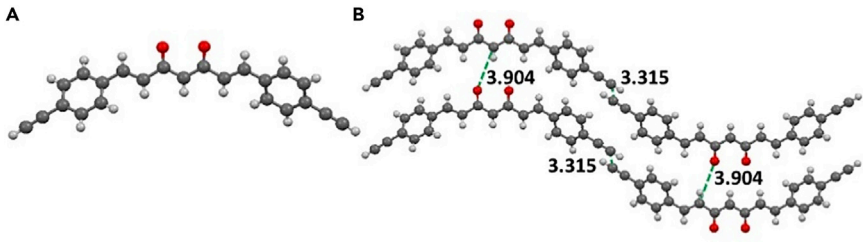

Figure 2. Molecular unit and packing motifs of AlkCCMoid (1)

(A) Molecular structure of 1-SC and (B) supramolecular packing. C atoms are in dark grey, O in red, and H in light gray, respectively. Depicted distances are in Angstrom (Å).

distances of the diketone moiety appear averaged (1.294 Å) and alternating C-C and C=C distances in the linear skeleton between 1.345 and 1.464 Å. As expected, the terminal alkyne groups exhibit the shortest distances, with C≡C lengths of 1.200 Å. The entire molecule presents a smooth sinusoidal shape due to the twisting of the aromatic rings and triple bonds from the plane of the backbone of the molecule, displaying a total length of 20.74 Å (H···H). The supramolecular arrangement shows the combination of two networks of molecular units in opposite directions (Figure 2B), with intermolecular interactions between the units in the same direction through O atoms from the β-diketone moiety of one molecule and the methine group (H-C) of the neighbor further ahead, with distances of 3.904 Å and angles close to 155°, and additional interactions arising through the triple bonds between molecules in opposite directions (C-C distances of 3.315 Å, Figure 2) creating 2D supramolecular networks.

In addition, 1-MP sublimates at 160 °C and 1 mbar of pressure, agreeing well with the thermogravimetric analysis (TGA) and differential scanning calorimetry (DSC, Figure S15). Taking this into account, we directly deposited our CCMoid onto Au(111) and Si/SiO_2 surfaces (1-SUB) using our specially designed sublimation system (Figure 1B and STAR Methods). Briefly, the solid is added to the bottom of a ground glass vessel, which is coupled to a stopcock adapter connected to a vacuum pump. Inside, a cylinder acting as a frame supports the surface to be studied, orienting it toward the solid. We carried out our experiments by fixing the distance between the solid and substrate, as well as the temperature, at 160 °C, while studying the effect of time (1, 2, 6, and 24 h) on the deposition process by Raman spectroscopy and Scanning Electron Microscopy (SEM). For long periods (>6 h), the evolution of the sublimation process collapses due to side reactions of the bulk solid at the bottom of the sublimation system. This is accompanied by a color change of the solid at the bottom, from yellow to brown, most likely due to the presence of polymeric species of CCMoid units bound through ethylene bonds, which gives rise to amorphous and insoluble materials.[44–46] However, our Raman studies indicated non-destructive deposition of the sublimated molecules on both types of substrates (Figures S17 and S18). For this purpose, control experiments were performed by depositing 1-MP by drop casting on the two surfaces. All samples showed the distinct C≡C-H vibrational band at 2100 cm^{-1}, plus additional ones at 1640 and 1600 cm^{-1} corresponding to the C=C and C=O vibrations, respectively, of the CCMoid skeleton.[47,48]

The morphology of 1-SUB on Au(111) and Si/SiO_2 was analyzed by SEM On the Au substrate, aggregates of different shapes (Figure S19) and sizes are formed (some of them with a lateral dimension greater than 30 μm). In contrast to the irregular assembly obtained on Au, the deposition on Si/SiO_2 leads to the formation of regular and elongated microstructures (Figure 3), with some of them exceeding 100 μm in length.

Topographical data acquired by atomic force microscopy (AFM) provided an amplified view confirming the formation of microcrystals with a wide variation in heights exposing flat surfaces (Figures S20-22), concluding that the CCMoid molecules tend to show better organization on Si/SiO_2 than on Au, displaying facetted microcrystals.

As mentioned earlier, molecular packing, crystal structure, and the interplay between molecular structure and substrate surfaces have an important impact on the electrical properties of materials.[49–52] To gain insight into the correlation between the AlkCCMoid structure with its electrical properties we used 1-SC, 1-MP, and 1-SUB (onto Si/SiO_2 surfaces) to perform XRD, GIWAXS, and electrical measurements.

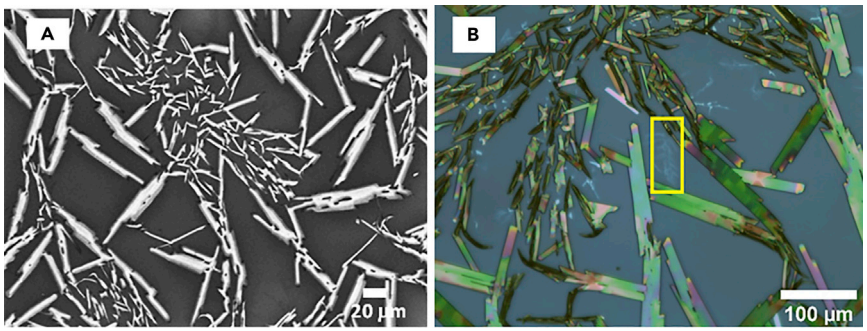

Figure 3. Microscopy information at the micro- and macroscale

(A) SEM and (B) optical microscope images of 1-sub sublimated over Si/SiO_2. Yellow inset shows fuzzy branched sheet-like structures, as a first stage toward the creation of microcrystals.

In this regard, Figure 4A compares specular XRD (theta-2theta) obtained for 1-MP (black) and 1-SUB (red) with the calculated from 1-SC (blue). The pattern belonging to 1-SC displays the diffracted intensity from the family of {200} crystalline planes and the (200) peak corresponds to 19.65 Å in the real space (at 2theta ≈ 4.5°, the momentum transfer equals to q = 0.3198 $Å^{-1}$). In the comparison of the three systems, important differences are found for 1-SUB, for which two phases were clearly visible (Figure 4A, red), with peak positions shifted to lower angles with respect to the XRD reflections of the single crystals (1-SC, blue), indicating the existence of two polymorphs. These two are observed in the case of 1-MP (Figure 4A, black), with one of them appearing as a small shoulder (*), again differing from the single-crystal pattern.

1-SUB on Si/SiO_2 was characterized also by GIWAXS to determine the orientation of the crystallites on the sample (Figure 4B). The observation of the Bragg peak (and higher diffraction order peaks) along the specular direction reveals a defined preferential orientation of the microcrystals that agrees with the flat facets observed in the morphology (Figure 3). On Au (111) a similar structure is observed but with a larger angular distribution of crystallite orientations, i.e. more orientation disorder (Figure S22).

In addition, we performed an XRD analysis of the XRD data collected for 1-MP. Based on observed reflections and systematic absences, we finally indexed the powder pattern to the *C2/m* space group and extracted the unit-cell parameters through Pawley refinements of the PXRD pattern of the sample (see Table S4 and Figure S31).

In parallel, to test the electrical properties of this CCMoid, high-quality 1-SC were selected with an optical microscope and transferred electrostatically to a Si/SiO_2 substrate (Figure 5A inset), using graphite paste

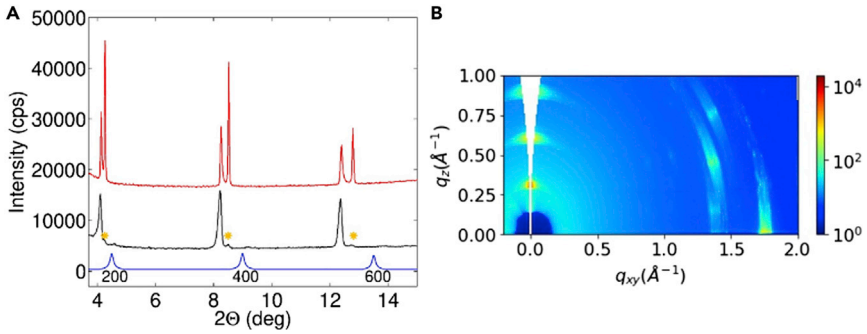

Figure 4. Collection of diffraction images

(A) Specular XRD measurements (th-2th) showing the comparison of the structure in 1-SC (blue), 1-MP (black), and 1-SUB (red) deposited on Si/SiO_2.

(B) 2D GIWAXS measured on the sample obtained by sublimation on Si/SiO_2 (1-SUB).

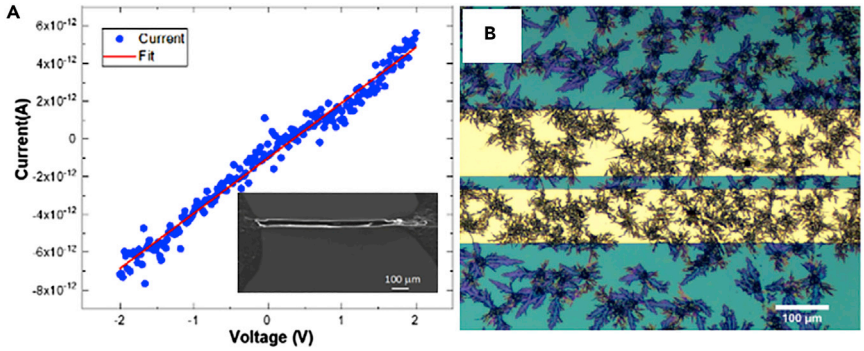

Figure 5. DC electrical measurements and device pictures

(A) Current-Voltage characteristics of a 1-SC electrically connected with graphite electrodes. Inset shows an SEM image of the single crystal.

(B) Electrodes connected by molecular ensembles sublimated on pre-patterned substrates.

to electrically connect both ends of the needle-shaped crystals. From the measured current-voltage characteristics done under vacuum, a conductivity value of about (8.50 $\pm$ 0.03)$\times 10^{-10}$S/cm was derived. The application of a gate voltage of $V_G = \pm$ 40V did not significantly alter the sample conductivity (Figure S23), indicating that single crystals were insulating in nature (Figure 5).[53] Similar conductivity values, measured in air and vacuum, were also obtained for 1-SUB samples (Figures 5B and S23), which are in good agreement with the DC conductivity values already reported for CCMoid films.[54]

To further characterize the dielectric properties of the AlkCCMoid broadband dielectric spectroscopy measurements were carried out using 1-MP and the setup described in STAR Methods and in SI (Figure S25). Briefly, a 1-MP pellet was loaded into a capacitor cell and measured as prepared and after storage, under ambient conditions, sandwiched between two aluminum contacts, for about one week. Our results indicate that while the electrical ac-conductivity displays only negligible changes, the extracted relative permittivity, shows a clear decrease at low frequencies. Changes in this region can be attributed to variations of the relative humidity. At high frequency (f > 100 kHz), the relative permittivity exhibited stable values (3.7 $\pm$ 0.1) when comparing samples measured as prepared and after 7 days of storage in air, respectively. Thus, the 1-MP is highly stable under ambient conditions, exhibiting permittivity values in good agreement with those found in the literature for small, conjugated molecules.[55]

However, this was not the case in the measurements of the electrical properties of the 1-MP pellet after soft annealing at temperatures ranging from 15°C < T < 55°C (SI). Figures S26–S30 and S6A show the evolution of impedance, phase, conductivity, and permittivity following heating and cooling, and Table S3 summarizes the trends for the parameters extracted from the measurements. We could notice that all values show small and reversible changes with temperature, except in the case of permittivity, for which a consistent and irreversible increase was observed, as shown in Figure 6A. This led us to hypothesize that the variation of the latter could be due to a thermally induced structural change in the morphology of 1-MP, based on the facts that conductance and capacitance are inversely proportional to sample thickness (i.e., pellet thickness), and the sample exhibited only modest and reversible variations in the case of the conductance.

To test our theory, we started by measuring the specular X-ray diffraction of the pristine microcrystalline powder and compared it with the same sample, after mild annealing, recovered from the capacitance measurement cell. Figure 6B displays the corresponding diffraction patterns from the sample before (black) and after annealing (red), where the diffractogram of the single-crystal, 1-SC, is given for comparative reasons (blue). The comparison clearly shows that, in general, the annealed 1-MP sample follows the same pattern, but also exhibits additional structural features of the single crystal, 1-SC. Hence, our findings reinforced the idea of structural changes affecting the permittivity parameter leading to theoretical calculations to provide further information.

DFT calculations were performed to calculate the permittivity values of 1-SC and that from the main polymorph found in 1-MP The calculations were performed with the all-electron FHI-aims computer code (*tight*

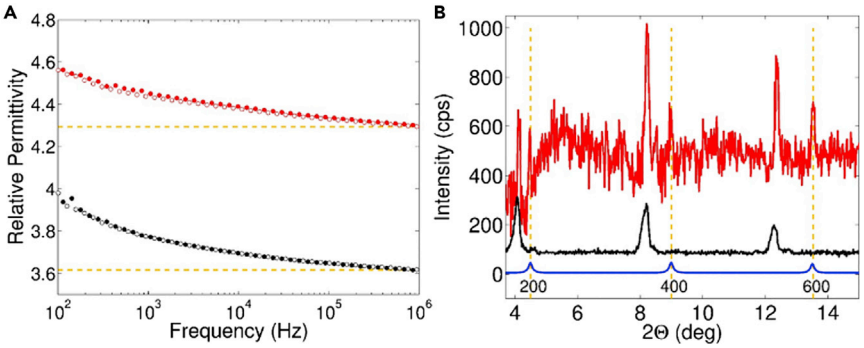

Figure 6. Dielectric and structural properties of AlkCCMoid (1)

(A) Relative permittivity of 1-MP, before (black) and after annealing (red), both measured at room temperature. Open and closed symbols correspond to forward and reverse frequency sweeps, respectively.

(B) Specular X-ray diffraction pattern of 1-MP before (black) and after annealing (red) compared to 1-SC (blue).

option for basis set and 24/12 k-points for small *Cc* and large *C2/m* unit cells, respectively).[56] The unit cell optimizations and dielectric properties, using Density Functional Perturbation Theory (DFPT),[57] were carried out using the PBE exchange-correlation functional,[58] including many-body dispersion contributions[59] (CIF files of the optimized structures, Data S1). The AlkCCMoid structure (1-SC_{theor}) was optimized using 1-SC data with and without symmetry constrain, as a starting point to maintain the same unit cell symmetry (Tables S2 and S5), showing an excellent agreement with the experimental data. The calculated dielectric constant (relative permittivity, see Table S6) for both optimized structures (with and without constrains) was the same, 3.85. This value is slightly different from the experimental value observed for 1-MP after annealing (~4.29 at high frequency, Figure 6A, red) because the precision limit of the DFPT approach is only implemented with the LDA (local density approximation) and GGA (generalized gradient approximation) functionals. Taking into account that the experimental XRD analysis after annealing of 1-MP indicated the existence of the two polymorphs (1-MP/1-SC, Figure 6B, red), the optimized structure for the main polymorph found in the 1-MP sample was initially set by fixing the unit-cell parameters based on the XRD analysis (Table S4). However, the subsequent full optimization, 1-MP_{theor}, gave the same structure, 1-MP, because the calculated gradient was below the convergence tolerances. The comparison between 1-MP_{theor} and 1-SC shows a considerable increase in volume for the former (around 21%, Table S4), being less stable by 8.3 kcal/mol per molecule. Therefore, the calculated dielectric constant for this system, 2.92, was consistent with the lower value found in the experimental data (~3.62 at high frequency, Figure 6A, black). In addition, the bandgaps calculated at PBE level of the 1-MP_{theor} compared to that of the 1-SC_{theor} were very similar, around 2 eV, being the latter only 0.1 eV larger than the former (Figure S33). This result corroborates our hypothesis that changes in permittivity values are due to structural variations, since bandgap and dielectric constant are usually inversely proportional.[60]

Summarizing, we have presented a comprehensive study of the structural and electrical properties of a new CCMoid, the AlkCCMoid (1). To this end, we have characterized our solid-state system in detail, emphasizing single and powder XRD data (1-SC and 1-MP, respectively), together with XRD data from the sublimation of AlkCCMoid directly onto different substrates (1-SUB), which includes FETs, by using a homemade sublimation system.

The electrical properties extracted from 1-SC and 1-SUB (using a FET device architecture) agree with and confirm the dielectric nature of the system. Detailed electrical characterization using 1-MP pellets provided obvious differences in permittivity before and after mild temperature and pressure conditions were applied to the sample. Subsequent structural analysis by powder XRD allowed us to observe a partial transition of the polymorphic 1-MP system to a mixture of polymorphs, 1-MP/1-SC. DFT calculations have corroborated the hypothesis relating the permittivity changes to those involving the existence of different polymorphs. Our findings are applicable to other molecules and provide the necessary tools to deposit and study molecules directly on surfaces as well as to understand new molecular-based systems, where polymorphism and electronics go along together.

Limitations of the study

Our future work may include similar studies, using a range of temperatures and including fluorescence experiments. Our sublimation methodology cannot yet provide precise control of the amount of material deposited, as do UHV-STM and related techniques, however, it can be tuned by controlling sublimation time, temperature, and pressure, and the basic three-terminal devices can be fabricated *in situ*, allowing pre-testing of the electronic properties of the molecules.

STAR★METHODS

Detailed methods are provided in the online version of this paper and include the following:

- KEY RESOURCES TABLE
- RESOURCE AVAILABILITY
  - Lead contact
  - Material availability
  - Data and code availability
- METHOD DETAILS
  - Synthetic methodology
  - Molecular characterization
  - Devices fabrication
  - GIWAXS experiments
  - Theoretical details
  - Additional instruments for characterization
- ADDITIONAL RESOURCES
  - Sublimation system

SUPPLEMENTAL INFORMATION

Supplemental information can be found online at https://doi.org/10.1016/j.isci.2022.105686.

ACKNOWLEDGMENTS

This work has received funding from the European Research Council (ERC) under the European Union's Horizon 2020 R&D program (ERC-724981). This work was also supported by the projects PID2019-108794GB-I00, GENESIS PID2019-111682RB-I00, PID2019-110907GB-I00, and PID2021-122464NB-I00 funded by MCIN/AEI/10.13039/501100011033 from the Ministerio de Ciencia e Innovación. E.C.S. acknowledges the financial support from the Spanish Government, (Grant PGC2018-098630-B-I00). R.P. acknowledges support from the Ramón y Cajal Fellowship (Ref. RyC2019-028474-I). J.dS. thanks to the MChem program of the University of Southampton. E.R. thanks Generalitat de Catalunya by a ICREA Academia award, Spanish Ministry Science for a Maria de Maeztu excellence grant (MDM-2017-0767), and computer resources, technical expertise and assistance provided by the Barcelona Supercomputing Center. R.M. thanks "la Caixa" Foundation (ID 100010434) for a Junior Leader fellowship (LCF/BQ/PI22/11910024). The crystal structures were collected at beamline XALOC at ALBA Synchrotron (Exp. 2017042211). The CSIC authors acknowledge the financial support from the Spanish Ministry Science, through the "Severo Ochoa" Programme for Centres of Excellence (FUNFUTURE,2020-2023). GIWAXS experiments were performed at the beam line BL11 – NCD-SWEET at ALBA Synchrotron with the collaboration of ALBA staff ; we also thank the support from Alba Cazorla.

AUTHORS CONTRIBUTIONS

D.R.L., D.H., and J.dS. investigation, data collection, and data analysis-molecular synthesis and characterization; R.Z. conceptualization, investigation, data collection, and data analysis-Raman spectroscopy, electrical, optical, and SEM characterization; E. B. and F.S. data collection and analysis- GIWAXS; E.B., R.M., E.C.S. data analysis-crystallography, and XRD Patterns; R.P. and M.M. data collection and data analysis-dielectric measurements; E.R. investigation, data collection, and data analysis-theoretical study; R.P., A.G.C., and N.A.A. conceptualization, investigation, data analysis, validation, supervision; A.G.C. and N.A.A. project administration and funding acquisition. All authors contributed to the writing and editing of the article.

DECLARATION OF INTERESTS

Regarding the sublimation system, a patent application has been filed (22/02/2022), with application number: P202230143 (Ref. Number: ES1641.1728). D.H., A.G.C., and N.A.A. are listed as co-inventors of the patents. The rest of the authors declare no competing interests.

Received: October 9, 2022
Revised: November 11, 2022
Accepted: November 28, 2022
Published: December 22, 2022

REFERENCES

1. Sheats, J.R. (2004). Manufacturing and commercialization issues in organic electronics. J. Mater. Res. *19*, 1974–1989. https://doi.org/10.1557/JMR.2004.0275.

2. Fleet, L.R., Stott, J., Villis, B., Din, S., Serri, M., Aeppli, G., Heutz, S., and Nathan, A. (2017). Self-assembled molecular nanowires for high performance organic transistors. ACS Appl. Mater. Interfaces *9*, 20686–20695. https://doi.org/10.1021/acsami.7b01449.

3. Tang, F., Wu, Z., Yang, C., Osenberg, M., Hilger, A., Dong, K., Markötter, H., Manke, I., Sun, F., Chen, L., and Cui, G. (2021). Synchroton X-ray tomography for rechargeable battery research: fundamentals, setups and applications. Small Methods *5*, 2100557. https://doi.org/10.1002/smtd.202100557.

4. Jones, A.O.F., Chattopadhyay, B., Geerts, Y.H., and Resel, R. (2016). Substate-Induced and thin-film phases: polymorphism of organic materials on surfaces. Adv. Funct. Mater. *26*, 2233–2255. https://doi.org/10.1002/adfm.201503169.

5. Reed, G., Littleton, M., Doran, H., Keay, K., Hughes, G.M., and Patrick, D.L. (2020). Bottom-up growth of shape-engineered molecular single crystals. Cryst. Growth Des. *20*, 5043–5047. https://doi.org/10.1021/acs.cgd.0c00194.

6. Taheri, H.E., Ocheje, M.U., St Onge, P.B.J., Rondeau-Gagné, S., and Mirhassani, M. (2021). Computational design of an integrated CMOS readout circuit for sensing with organic field-effect transistors. Front. Electron. *2*, 725008. https://doi.org/10.3389/felec.2021.725008.

7. Liu, R., Wang, Z.L., Fukuda, K., and Someya, T. (2022). Flexible self-charging power sources. Nat. Rev. Mater. *7*, 870–886. https://doi.org/10.1038/s41578-022-00441-0.

8. Qiu, X., and Chiechi, R.C. (2022). Printable logic circuits comprising self-assembled protein complexes. Nat. Commun. *13*, 2312. https://doi.org/10.1038/s41467-022-30038-8.

9. Lampe, V. (1918). Syntheses von curcumin. Ber. Dtsch. Chem. Ges. *51*, 1347–1355. https://doi.org/10.1002/cber.19180510223.

10. Pabon, H.J.J. (1964). A synthesis of curcumin and related compounds. Recl. Trav. Chim. Pays. Bas. *83*, 379–386. https://doi.org/10.1002/recl.19640830407.

11. Pedersen, U., Rasmussen, P.B., and Lawesson, S.O. (1985). Synthesis of naturally occurring curcuminoids and related compounds. Liebigs Ann. Chem. *1985*, 1557–1569. https://doi.org/10.1002/jlac.198519850805.

12. Zhang, Y., Tu, L., Lu, L., Li, Y., Song, L., Qi, Q., Song, H., Li, Z., and Huang, W. (2020). Screening and application of boron difluoride complexes of curcumin as colorimetric and radiometric fluorescent probes for bisulfite. Anal. Methods *12*, 1514–1521. https://doi.org/10.1039/D0AY00173B.

13. Gál, E., and Nagy, L.C. (2021). Photophysical properties and electronic structure of symmetrical curcumin analogues and their BF2 complexes including a phenothiazine substituted derivative. Symmetry *13*, 2299. https://doi.org/10.3390/sym13122299.

14. Cornago, P., Cabildo, P., Sanz, D., Claramunt, R.M., Torralba, M.C., Torres, M.R., and Elguero, J. (2013). Structures of hemi-curcuminoids in the solid state and in solution. Eur. J. Org. Chem. *2013*, 6043–6054. https://doi.org/10.1002/ejoc.201300488.

15. Abu-Dief, A.M., Díaz-Torres, R., Sañudo, E.C., Abdel-Rahman, L.H., and Aliaga-Alcalde, N. (2013). Novel sandwich triple-decker dinuclear Nd^{III}-(bis-N, N′-p-bromo-salicylidiene-1, 2-diaminobenzene) complex. Polyhedron *64*, 203–208. https://doi.org/10.1016/j.poly.2013.04.010.

16. Díaz-Torres, R., Menelaou, M., Roubeau, O., Sorrenti, A., Brandariz-De-Pedro, G., Sañudo, E.C., Teat, S.J., Fraxedas, J., Ruiz, E., and Aliaga-Alcalde, N. (2016). Multiscale study of mononuclear Co^{II} SMMs based on curcuminoid ligands. Chem. Sci. *7*, 2793–2803. https://doi.org/10.1039/C5SC03298A.

17. Rodríguez-Cid, L., Qian, W., Iribarra-Araya, J., Etcheverry-Berríos, Á., Martínez-Olmos, E., Choquesillo-Lazarte, D., Sañudo, E.C., Roubeau, O., López-Periago, A.M., González-Campo, A., et al. (2021). Broadening the scope of high dimensionality nanomaterials using pyridine-based curcuminoids. Dalton Trans. *50*, 7056–7064. https://doi.org/10.1039/d1dt00708d.

18. Olavarría-Contreras, I.J., Etcheverry-Berríos, A., Qian, W., Gutiérrez-Cerón, C., Campos-Olguín, A., Sañudo, E.C., Dulić, D., Ruiz, E., Aliaga-Alcalde, N., Soler, M., and van der Zant, H.S.J. (2018). Electric-field induced bistability in single-molecule conductance measurements for boron coordinated curcuminoids compounds. Chem. Sci. *9*, 6988–6996. https://doi.org/10.1039/c8sc02337a.

19. Aliaga-Alcalde, N., Marqués-Gallego, P., Kraaijkamp, M., Herranz-Lancho, C., den Dulk, H., Görner, H., Roubeau, O., Teat, S.J., Weyhermüller, T., and Reedijk, J. (2010). Copper curcuminoids containing anthracene groups: fluorescent molecules with cytotoxicity activity. Inorg. Chem. *49*, 9655–9663. https://doi.org/10.1021/ic101331c.

20. Menelaou, M., Ouharrou, F., Rodríguez, L., Roubeau, O., Teat, S.J., and Aliaga-Alcalde, N. (2012). Dy^{III} and Yb^{III}-Curcuminoid compounds: original fluorescent single-ion magnet and magnetic near-IR luminescent species. Chemistry *18*, 11545–11549. https://doi.org/10.1002/chem.201200955.

21. Aliaga-Alcalde, N., and Rodríguez, L. (2012). Solvatochromic studies of a novel Cd^{2+}-anthracene-based curcuminoid and related complexes. Inorg. Chim. Acta. *380*, 187–193. https://doi.org/10.1016/j.ica.2011.08.052.

22. Rodríguez-Cid, L., Sañudo, E.C., López-Periago, A.M., González-Campo, A., Aliaga-Alcalde, N., and Domingo, C. (2020). Novel Zn(II) coordination polymers based on the natural molecule bisdemethoxycurcumin. Cryst. Growth Des. *20*, 6555–6564. https://doi.org/10.1021/acs.cgd.0c00742.

23. Su, H., Sun, F., Jia, J., He, H., Wang, A., and Zhu, G. (2015). A highly porous medical metal-organic framework constructed from bioactive curcumin. Chem. Commun. *51*, 5774–5777. https://doi.org/10.1039/C4CC10159F.

24. Archet, F., Yao, D., Chambon, S., Abbas, M., D'Aléo, A., Canard, G., Ponce-Vargas, M., Zaborova, E., Le Guennic, B., Wantz, G., and Fages, F. (2017). Synthesis of bioinspired curcuminoid small molecules for solution-processed organic solar cells with high open-circuit voltage. ACS Energy Lett. *2*, 1303–1307. https://doi.org/10.1021/acsenergylett.7b00157.

25. Castro, E., Cerón, M.R., Garcia, A.H., Kim, Q., Etcheverry-Berríos, A., Morel, M., Díaz-Torres, R., Qian, W., Martinez, Z., Mendez, L., et al. (2018). A new family of fullerene derivatives: fullerene-curcumin conjugates for biological and photovoltaic applications. RSC Adv. *8*, 41692–41698. https://doi.org/10.1039/C8RA08334G.

26. Etcheverry-Berríos, A., Olavarría, I., Perrin, M.L., Díaz-Torres, R., Jullian, D., Ponce, I., Zagal, J.H., Pavez, J., Vásquez, S.O., Van der Zant, H.S.J., et al. (2016). Multiscale approach to the study of the electronic properties of two thiophene curcuminoid molecules. Chemistry *22*, 12808–12818. https://doi.org/10.1002/chem.201601187.

27. Portolés-Gil, N., Lanza, A., Aliaga-Alcalde, N., Ayllón, J.A., Gemmi, M., Mugnaioli, E., López-Periago, A.M., and Domingo, C. (2018). Crystalline curcumin bioMOF obtained by precipitation in supercritical CO2 and structural determination by electron diffraction tomography. ACS Sustain. Chem. Eng. *6*, 12309–12319. https://doi.org/10.1021/acssuschemeng.8b02738.

28. Choi, K.R., Kim, D.H., Lee, Y.U., Placide, V., Huynh, S., Yao, D., Canard, G., Zaborova, E., Mathevet, F., Mager, L., et al. (2021). Effect of the electron donating group on the excited-state electronic nature and epsilon-near-zero properties of curcuminoid-borondifluoride dyes. RSC Adv. *11*, 38247–38257. https://doi.org/10.1039/d1ra08025c.

29. Kim, D.H., D'Aléo, A., Chen, X.K., Sandanayaka, A.D.S., Yao, D., Zhao, L., Komino, T., Zaborova, E., Canard, G., Tsuchiya, Y., et al. (2018). High-efficiency electroluminescence and amplified spontaneous emission from a thermally activated delayed fluorescent near-infrared emitter. Nat. Photonics *12*, 98–104. https://doi.org/10.1038/s41566-017-0087-y.

30. D'Aléo, A., Sazzad, M.H., Kim, D.H., Choi, E.Y., Wu, J.W., Canard, G., Fages, F., Ribierre, J.-C., and Adachi, C. (2017). Boron difluoride hemicurcuminoid as an efficient far red to near-infrared emitter: toward OLEDs and laser dyes. Chem. Commun. *53*, 7003–7006. https://doi.org/10.1039/c7cc01786c.

31. Prins, F., Barreiro, A., Ruitenberg, J.W., Seldenthuis, J.S., Aliaga-Alcalde, N., Vandersypen, L.M.K., and Van der Zant, H.S.J. (2011). Room-temperature gating of molecular junctions using few-layer graphene nanogap electodes. Nano Lett. *11*, 4607–4611. https://doi.org/10.1021/nl202065x.

32. Burzurí, E., Island, J.O., Díaz-Torres, R., Fursina, A., González-Campo, A., Roubeau, O., Teat, S.J., Aliaga-Alcalde, N., Ruiz, E., and Van der Zant, H.S.J. (2016). Sequential electron transport and vibrational excitations in an organic molecule coupled to few-layer graphene electrodes. ACS Nano *10*, 2521–2527. https://doi.org/10.1021/acsnano.5b07382.

33. Island, J.O., Holovchenko, A., Koole, M., Alkemade, P.F.A., Menelaou, M., Aliaga-Alcalde, N., Burzurí, E., and Van der Zant, H.S.J. (2014). Fabrication of hybrid molecular devices using multi-layer graphene break junctions. J. Phys. Condens. Matter *26*, 474205. https://doi.org/10.1088/0953-8984/26/47/474205.

34. Xiang, D., Jeong, H., Lee, T., and Mayer, D. (2013). Mechanically controllable break junctions for molecular electronics. Adv. Mater. *25*, 4845–4867. https://doi.org/10.1002/adma.201301589.

35. Perrin, M.L., Burzurí, E., and Van der Zant, H.S.J. (2015). Single-molecule transistors. Chem. Soc. Rev. *44*, 902–919. https://doi.org/10.1039/c4cs00231h.

36. Díaz-Torres, R., Menelaou, M., González-Campo, A., Teat, S., Sañudo, E., Soler, M., and Aliaga-Alcalde, N. (2016). Comparative magnetic studies in the solid state and solution of two isostructural 1D coordination polymers containing CoII/NiII-curcuminoid moieties. Magnetochemistry *2*, 29. https://doi.org/10.3390/magnetochemistry2030029.

37. Lorenz, M., Ramachandra Rao, M.S., Venkatesan, T., Fortunato, E., Barquinha, P., Branquinho, R., Salgueiro, D., Martins, R., Carlos, E., Liu, A., et al. (2016). The 2016 oxide electronic materials and oxide interfaces roadmap. J. Phys. D Appl. Phys. *49*, 433001. https://doi.org/10.1088/0022-3727/49/43/433001.

38. Menelaou, M., Weyhermüller, T., Soler, M., and Aliaga-Alcalde, N. (2013). Novel paramagnetic-luminiscent building blocks containing manganese (II) and anthracene-based curcuminoids. Polyhedron *52*, 398–405. https://doi.org/10.1016/j.poly.2012.08.061.

39. Rieger, R., and Müllen, K. (2010). Forever young: polycyclic aromatic hydrocarbons as model cases for structural and optical studies. J. Phys. Org. Chem. *23*, 315–325. https://doi.org/10.1002/poc.1644.

40. Tauc, J. (1968). Optical properties and electronic structure of amorphous Ge and Si. Mater. Res. Bull. *3*, 37–46. https://doi.org/10.1016/0025-5408(68)90023-8.

41. Viezbicke, B.D., Patel, S., Davis, B.E., and Birnie, D.P. (2015). Evaluation of Tauc method for optical absorption edge determination: ZnO thin films as a model system. Phys. Status Solidi B *252*, 1700–1710. https://doi.org/10.1002/pssb.201552007.

42. Makuła, P., Pacia, M., and Macyk, W. (2018). How to correctly determine the band gap energy of modified semiconductor photocatalyst based on UV-Vis spectra. J. Phys. Chem. Lett. *9*, 6814–6817. https://doi.org/10.1021/acs.jpclett.8b02892.

43. Michaelson, H.B. (1977). The work function of the elements and its periodicity. J. Appl. Phys. *48*, 4729–4733. https://doi.org/10.1063/1.323539.

44. Albrecht, F., Rey, D., Fatayer, S., Schulz, F., Pérez, D., Peña, D., and Gross, L. (2020). Intramolecular coupling of terminal alkynes by atom manipulation. Angew. Chem., Int. Ed. Engl. *59*, 22989–22993. https://doi.org/10.1002/anie.202009200.

45. Gao, H.Y., Wagner, H., Zhong, D., Franke, J.H., Studer, A., and Fuchs, H. (2013). Glaser coupling at metal surfaces. Angew. Chem., Int. Ed. Engl. *52*, 4024–4028. https://doi.org/10.1002/anie.201208597.

46. Ciampi, S., James, M., Darwish, N., Luais, E., Guan, B., Harper, J.B., and Gooding, J.J. (2011). Oxidative acetylenic coupling reactions as a surface chemistry tool. Phys. Chem. Chem. Phys. *13*, 15624–15632. https://doi.org/10.1039/C1CP21450K.

47. Miloudi, L., Bonnier, F., Bertrand, D., Byrne, H.J., Perse, X., Chourpa, I., and Munnier, E. (2017). Quantitative analysis of curcumin-loaded alginate nanocarriers in hydrogels using Raman and attenuated total reflection infrared spectroscopy. Anal. Bioanal. Chem. *409*, 4593–4605. https://doi.org/10.1007/s00216-017-0402-y.

48. Kolev, T.M., Velcheva, E.A., Stamboliyska, B.A., and Spiteller, M. (2005). DFT and experimental studies of the structure and vibrational spectra of curcumin. Int. J. Quant. Chem. *102*, 1069–1079. https://doi.org/10.1002/qua.20469.

49. Peng, B., Wu, R., and Li, H. (2021). Crystallization from a Droplet: single-crystalline arrays and heterojunctions for organic electronics. Acc. Chem. Res. *54*, 4498–4507. https://doi.org/10.1021/acs.accounts.1c00537.

50. Ryu, H.S., Kim, M.J., Lee, Y.W., Lee, S.H., Shin, T.J., Cho, J.H., and Woo, H.Y. (2019). Synthesis, molecular packing, and electrical properties of new regioisomeric n-type semiconducting molecules with modification of alkyl substituents position. ACS Appl. Mater. Interfaces *11*, 47170–47181. https://doi.org/10.1021/acsami.9b17664.

51. Kiriy, N., Kiriy, A., Bocharova, V., Stamm, M., Richter, S., Plötner, M., Fischer, W.J., Krebs, F.C., Senkovska, I., and Adler, H.J. (2004). Conformation, molecular packing, and field effect mobility of regioregular b, b'-dihexylsexithiophene. Chem. Mater. *16*, 4757–4764. https://doi.org/10.1021/cm049686a.

52. Mas-Torrent, M., and Rovira, C. (2011). Role of molecular order and solid-state structure in organic field-effect transistors. Chem. Rev. *111*, 4833–4856. https://doi.org/10.1021/cr100142w.

53. Sun, L., Park, S.S., Sheberla, D., and Dincă, M. (2016). Measuring and reporting electrical conductivity in metal-organic frameworks: Cd2(TTFTB) as a case study. J. Am. Chem. Soc. *138*, 14772–14782. https://doi.org/10.1021/jacs6b09345.

54. Dakhel, A.A., Jasim, K.E., Cassidy, S., and Henari, F.Z. (2013). Extraction and dielectric properties of curcuminoid films grown on Si substrate for high-k dielectric applications. Mater. Sci. Eng., B *178*, 1062–1067. https://doi.org/10.1016/j.mseb.2013.06.003.

55. Hughes, M.P., Rosenthal, K.D., Ran, N.A., Seifrid, M., Bazan, G.C., and Nguyen, T. (2018). Determining the dielectric constants of organic photovoltaic materials using impedance spectroscopy. Adv. Funct. Mater. *28*, 1801542. https://doi.org/10.1002/adfm.201801542.

56. Blum, V., Gehrke, R., Hanke, F., Havu, P., Havu, V., Ren, X., Reuter, K., and Scheffler, M. (2009). Ab initio molecular simulations with numeric atom-centered orbitals. Comput.

Phys. Commun. *180*, 2175–2196. https://doi.org/10.1016/j.cpc.2009.06.022.

57. Shang, H., Raimbault, N., Rinke, P., Scheffler, M., Rossi, M., and Carbogno, C. (2018). All-electron, real-space perturbation theory for homogeneous electric, and application within DFT. New J. Phys. *20*, 073040. https://doi.org/10.1088/1367-2630/aace6d.

58. Perdew, J.P., Burke, K., and Ernzerhof, M. (1996). Generalized gradient approximation made simple. Phys. Rev. Lett. *77*, 3865–3868. https://doi.org/10.1103/PhysRevLett.77.3865.

59. Tkatchenko, A., DiStasio, R.A., Car, R., and Scheffler, M. (2012). Accurate and efficient method for many-body Van der Waals interactions. Phys. Rev. Lett. *108*, 236402. https://doi.org/10.1103/PhysRevLett.108.236402.

60. Choudhary, K., Garrity, K.F., Sharma, V., Biacchi, A.J., Hight Walker, A.R., and Tavazza, F. (2020). High-throughput density functional perturbation theory and machine learning predictions of infrared, piezoelectric, and dielectric responses. NPJ Comput. Mater. *6*, 64. https://doi.org/10.1038/s41524-020-0337-2.

STAR★METHODS

KEY RESOURCES TABLE

REAGENT or RESOURCE	SOURCE	IDENTIFIER
Chemicals		
Acetylacetone	Merck	P7754; CAS: 123-54-6
Boron trioxide	Merck	56,750; CAS: 1303-86-2
Tributyl borate	Merck	90,795; CAS: 688-74-4
N-butyl amine	Fischer Scientific, S.L.	10030462; CAS: 109-72-8
Ethynyl benzaldehyde	Fluorochem	MFCD05664348; CAS: 63697-96-1
4-[(Trimethylsilyl)ethynyl] benzaldehyde	Merck	523380; CAS: 77123-57-0
Potassium bromide	Merck	209619; CAS: 7758-02-3
Hydroclorhidric acid 37%	Carlo Erba	403871; CAS: 7647-01-0
Ethyl acetate	Carlo Erba	528299; CAS: 141-78-6
Methanol	Carlo Erba	528101; CAS: 67-56-1
Acetonitrile	Carlo Erba	P0060228; CAS: 75-05-8
Chloroform D 99.80%D	Eurisotop	D007HAG; CAS: 865-49-6
MilliQ water	Merck	purified with Milli-Q®EQ-700
Acetone	Chem-lab	CAS: 67-64-1
Isopropanol	Chem-lab	CAS: 67-63-0
Deposited data		
CIF file of system **1**	The Cambridge Crystallographic Data Centre	CCDC2206711
CIF file of system **2**	The Cambridge Crystallographic Data Centre	CCDC2206712
Software and algorithms		
OriginPro v.2018	http://originlab.com	
Mercury	http://ccdc.cam.ac.uk	
MNova v.2014	http://mestrelab.com	
MMass	http://mmass.org	
Python	https://www.python.org/	

RESOURCE AVAILABILITY

Lead contact

Further information and requests for resources and CCMoid molecules should be directed to and will be fulfilled by the lead contact, Núria Aliaga-Alcalde (nuria.aliaga@icrea.cat).

Material availability

Materials are available upon request.

Data and code availability

- CCDC 2206711 (**1**) and 2206712 (**2**), contain the supplementary crystallographic data. These data can be obtained free of charge by The Cambridge Crystallographic Data Centre.
- The rest of the data reported in this article are available within the paper and the supplemental information files.
- There is no code associated with this work.

METHOD DETAILS

Synthetic methodology

AlkCCMoid (**1**) and AlkTMSCCMoid, (**2**), were synthesized following a modification of the Pabonś method[10] according to the procedure shown in below scheme.

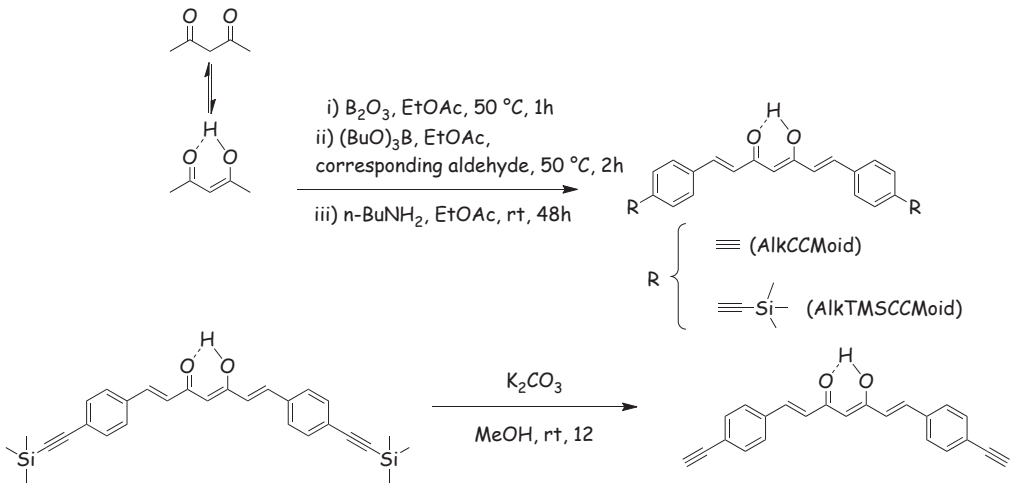

Synthetic paths in the achievement of 1 and 2

Synthesis of AlkCCMoid (**1**). Two synthetic routes (A and B) were used to obtain this molecule.

(A) 200 mg (2 mmol) of acac and 100 mg of B_2O_3 (0.7 eq, 1.4 mmol) were solubilized in 2 mL of EtOAc. The mixture was stirred and heated at 50 ºC for 1 h. Then 1.1 mL (4 mmol) of $(BuO)_3B$ was added, followed by the addition of a solution of 809 mg of 1-ethylbenzaldehyde (4 mmol) in 2 mL of EtOAc. The reaction was stirred at 50 ºC for 2 h and then cooled to room temperature. Next, a solution of *n*-$BuNH_2$ (100 µL, 1 mmol) in EtOAc (1.3 mL) was added dropwise and the reaction was stirred at room temperature for two days. Finally, an aqueous HCl solution (0.1 M) was added to the solution and the mixture was left stirring at 40 ºC for 1 h. The resulting precipitate was filtered off and washed with cold MeOH. Recrystallization was achieved by dissolving the solid in MeCN and leaving the solution in the refrigerator at 0 ºC. AlkCCMoid was obtained as a brown powder in 36% yield. ^{1}H NMR (δ in ppm, 360 MHz, $CDCl_3$): 15.83 (s, 1H), 7.64 (d, J = 15.8 Hz, 2H), 7.51 (s, 8H), 6.63 (d, J = 15.8 Hz, 2H), 5.85 (s, 1H), 3.20 (s, 2H). ^{13}C{^{1}H} NMR (δ in ppm, 90 MHz, $CDCl_3$): 183.2, 139.8, 135.4, 132.8 128.1, 125.1, 123.9, 102.4, 83.4, 79.4. ATR-FTIR (cm^{-1}): 3273 ($\nu_{\equiv C\text{-}H}$), 3033 ($\nu_{=C\text{-}H}$ and $\nu_{arC\text{-}H}$), 2958-2929 ($\nu_{\text{-}C\text{-}H}$), 2162 ($\nu_{\text{-}C\equiv C\text{-}}$), 1698 ($\nu_{C=O}$ β-diketone), 1629 (C=O β-diketone, with intermolecular H-bonds), 1495 ($\nu_{arC\text{-}C}$, skeleton vibrations), 1136 ($\delta_{ip\ ar\ C\text{-}H}$) 974 (δ CH) 822 ($\nu_{arC\text{-}H}$ ρ-disubstituted and $\delta_{oop\ CH}$), 623 ($\delta_{\equiv C\text{-}H}$). MS MALDI-TOF (m/z): calc. for $C_{23}H_{16}O_2$[M-1]: 323.1; found: 322.9. Elemental analysis calculated for AlkCCMoid·2MeCN ($C_{27}H_{22}N_2O_2$): C, 79.78; H, 5.46. Found: C, 79.35; H, 5.08.

(B) The second synthetic route is based on the preparation of the TMS-protected analog CCMoid (AlkTMSCCMoid, **2**) followed by the deprotection in basic media. Full details on the characterization of AlkTMSCCMoid (and AlkCCMoid) are provided in Figures S1–S17 and Tables S1 and S2. Therefore, 200 mg of **2** (2 mmol) and 590 mg of K_2CO_3 (20 mmol) were solubilized in 45 mL of MeOH and the mixture was stirred at room temperature overnight. Then, an aqueous HCl solution (0.1 M) was added, and the resulting solution was concentrated at the rotary evaporator. The final system was extracted with DCM and washed three times with 10 mL brine. AlkCCMoid was obtained without further purification as a brown powder in 70% yield.

Molecular characterization

Tauc's plot of UV-VIS

In solid state, using Tauc's mathematical extrapolation[40,41] estimated band gap values were obtained for AlkCCMoid (**1**) and AlkTMSCCMoid (**2**), respectively. In both cases, these values were obtained by averaging the results of the direct and indirect allowed transitions.

$$(\alpha * h * \nu)^{\frac{1}{n}} = B * (h * \nu - E_g) \quad \text{(Equation 1)}$$

Where:

- α = 2.303·Abs/l (absorption coefficient)
- l = sample thickness
- n = ½ for direct allowed transitions and 2 for indirect allowed transitions

(Figure S11)

Electrochemistry[42]

Using the differential pulse voltammetry (DPV), we calculated the E_g^{ec}.

We used Equations 2 and 3 to calculate the energy of the HOMO and LUMO vs. the ferrocene molecule under vacuum conditions:

$$E_{HOMO} = -\left((E_{onset})^{(oxid)}\right) + 4.8\ eV \quad \text{(Equation 2)}$$

$$E_{LUMO} = -\left((E_{onset})^{(red)}\right) + 4.8\ eV \quad \text{(Equation 3)}$$

The value of 4.8 eV corresponds to the potential of the Fc/Fc^+ couple at the vacuum level. Finally, the energy gap is calculated by:

$$E_g^{ec} = (E_{LUMO}) - (E_{HOMO})\ eV \quad \text{(Equation 4)}$$

(Figures S12 and S13 and Table S1).

Devices fabrication

FETs

Three-terminal devices were fabricated on silicon substrates coated with 300 nm of thermal oxide. A layer of the positive Microposit® resist S1813 by Shipley® was spin coated at 4000 rpm to achieve a final thickness of 1.4 μm and dried during 1 min on a hot plate at 95°C. Then, it was exposed under a 385 nm semiconductor light source using the micro-writer ML3 by Durham Magneto Optics Ltd working at an intensity of 150 mJ/cm^2. Resist development was carried out by dipping the sample in the Microposit® MF 319 developer solution during 40 sec stopped in milliQ water for 30 s and finally dried under a N_2 flow. Thereafter an adhesion layer of Cr with a thickness of 5 nm was evaporated in the evaporation system Auto 360 from Boc Edwards followed by 50 nm of Au. The resulting Au pattern was then revealed through lift-off by immersing the samples in an acetone bath during few minutes followed by rinsing with acetone and isopropanol and dried under a N_2 flow.

The DC electrical characterization of three-terminal devices with sublimated molecules was carried out in a Probe Station by Lakeshore at ambient condition and under vacuum by using two system measurement units (SMU) 2450 from Keithley and a home-made python routine. Resistance measurements were done recording 2 probes current-voltage characteristics applying back and forward voltage sweeps in the range between ±1V. The electrical characterization of the FET was performed under vacuum and applying gate-source voltage V_{GS} between ±40V to the bottom Si acting as a gate electrode. AC electrical characterization was carried out by employing a Novocontrol alpha-A Impedance Analyzer. Temperature sweeps were carried out employing a *Peltier* element which was connected to a PID temperature controller for temperature stabilization.

Sublimated CCMoid-FET setup

The resistivity of the molecular assembly embedded between interdigitated electrodes was obtained from standard 2 probes current-voltage measurements that were operated in air and under vacuum using a

Probe Station from Lakeshore (Figure S23). Under both environmental conditions I(V) data were rather scattered, however for some of the curves (I_g1 and I_g7) it was possible to fit the data to a linear relationship with strong correlation values ($r > 0.85$). We used the values of the resistance obtained by the linear fit to the measured I(V) to evaluate the resistivity according to the Equation 5

$$\rho = \frac{RA}{l} \quad \text{(Equation 5)}$$

Where A is the area (A = W*d, W channel width and d sample thickness, respectively) while l is the channel length of the area between the electrodes covered by the molecules. From this, we obtain for ρ(g1) a value of $6.5 \times 10^4\ \Omega\cdot$m and $3.7 \times 10^5\ \Omega\cdot$m for ρ(g7).

Sample preparation for microcrystalline powder (1-MP) measurements

1-MP was ground very fine by employing mortar and pestle under ambient conditions (RH = 45 ± 5%, T = 25 ± 5°C). The powder was loaded into a homemade capacitor cell consisting of Aluminum (~ 35 μm) bottom and top contacts mounted on polycarbonate sheets with about 100 μm thickness (setup, including dimensions in Figure S25). Electrical connections were arranged on opposite sides of the capacitor to avoid high frequency coupling. After loading the cell, it was sandwiched between two rubber pieces and a hydrostatic pressure of about 175 ± 20 kPa was applied. Electrical characterization was carried out by employing a Novocontrol alpha-A Impedance Analyzer. Temperature sweeps were controlled employing a Peltier element which was connected to a PID temperature controller for temperature stabilization. Cell calibration was done by employing a polyimide sheet, *vide infra*.

Calibration of the measurement cell

The measurement cell was calibrated employing a sheet of polyimide with a thickness of d = 125 ± 5 μm, sandwiched between the aluminum contacts. Table S3 and figure S27 show electrical parameters extracted for the broadband dielectric spectroscopy *i.e.* |Impedance|, Phase, Capacitance and Conductivity. Figure S28 shows the calculated relative permittivity of polyimide. The high relative permittivity value at low frequency can be attributed to moisture, since the measurement was done under ambient conditions. At high frequency the relative permittivity converges to a value of: $\varepsilon_r = 3.6 \pm 0.1$, which is in good agreement with literature.

GIWAXS experiments

GIWAXS experiments were performed at the BL11 - NCD-SWEET beamline of the Synchrotron ALBA (Bellaterra, Spain). The energy of the synchrotron X-ray radiation was 14.4 keV. The images (diffraction patterns) were collected with an Rayonix LX255HS area detector. Ten images were collected (exposure time of 0.2 s) and summed up to improve signal-to-noise ratio. The substrates were measured at different incident angles (from 0.09° up to 0.15°), where the data in the Figure 4A corresponds to an incident angle of 0.09° (below the critical angle of the substrate). The data are converted to reciprocal space maps with the out-of-plane (qz) and in-plane (qr) components of the scattering vector corresponding to the directions perpendicular and parallel to the surface, respectively.

Theoretical details

The theoretical permittivity values of **1-SC** and the main polymorph found in **1-MP** were calculated. The DFT calculations were carried out with the all-electron FHI-aims computer code (*tight* option for basis set and 24/12 k-points for small *Cc* and large *C2/m* unit cells, respectively).[56] The unit cell optimizations and dielectric properties, using Density Functional Perturbation Theory (DFPT),[57] were performed using the PBE exchange-correlation functional,[58] including many-body dispersion contributions[59] (Figure S33 and Tables S5and S6).

Additional instruments for characterization

Single crystal X-ray diffraction data for AlkCCMoid (**1**) and AlkTMSCCMoid (**2**) were collected at the XALOC beamline 13 of Alba-CELLS Synchrotron (Spain). Data for **1** using a Bruker D8 Venture diffractometer at 293 K (λ = 0.72932 Å).

The simulated powder patterns were calculated from the single crystal crystallographic data using Mercury 3.7 software. Peak indexing and space-group determination based on X-ray diffraction patterns were performed using the DICVOL5 algorism in Material Studio 8.0 and checked with GSAS-II software. Pawley refinements were performed using GSAS-II software.

Fourier transform infrared (FTIR) spectra were obtained using an FT-IR JASCO 4700LE using the ATR (attenuated total reflectance) accessory in the range between 500 and 4000 cm^{-1}, 2 mg of the powdered samples were deposited covering the crystal of the ATR accessory and pressed with the pressure tip.

Elemental analyses were carried out using a PerkinElmer 2400 series II analyzer.

^{1}H-NMR and ^{13}C-NMR spectra were obtained on a Bruker Advanced at 360 MHz and 298 K.

Thermogravimetric analysis was performed under a N_2 atmosphere from room temperature to 1000 °C at a heating rate of 10 °C min^{-1}, using a simultaneous thermogravimetric analysis (TG)-differential scanning calorimetry/differential thermal analysis (heat flow DSC /DTA) system NETZSCH-STA 449 F1 Jupiter.

MALDI-TOF mass spectra were recorded with an ULTRAFLEXTREME mass spectrometer (Bruker) at Servei de Proteòmica i Biologia Estructural (SePBioEs) from UAB.

UV/Vis absorption spectra of liquid samples were obtained with a Varian Cary 780 spectrometer by using quartz cells with operating range of 200–600 nm, mainly in reflectance or transmittance mode. For solid samples the Diffuse Reflectance Sphere DRA-2500 accessory of a Varian Cary 780 UV/Vis/NIR spectrophotometer was used with operating range of 200–700 nm, mainly in reflectance or transmittance mode.

Raman scattering spectra were measured on a XploraTM Plus system from Horiba Scientific model with a solid-state laser, emitting at 785 nm wavelength. The laser power at the sample was about 10% of 5 mW.

SEM images of molecules sublimated on different surfaces were obtained with a Zeiss Auriga 40 Field Emission microscope at an acceleration voltage of 2kV and a working distance below 4 mm without metallization of the samples.

ADDITIONAL RESOURCES

Sublimation system

Regardless of the method, optimization of practical procedures is crucial to facilitate the screening of the electronic properties of molecules in order to provide faster feedback for redesigning more efficient molecular-based devices. Here, we propose an alternative option in the molecular deposition stage, in which the sublimated material is deposited directly onto the desired substrate or device operating under the conditions that conventional sublimation systems do, using a homemade setup capable of operating in low-medium vacuum conditions. Our design allows for direct use in standard laboratories, with the advantage of one-step deposition of the sublimated material on a variety of surfaces/substrates and pre-formed devices. In addition, the use of common glassware components, together with plastic support parts, make the entire system affordable for conventional characterizations and easily repairable, replaceable, or modifiable.

The solid is added to the bottom of a ground glass vessel, which is coupled to a stopcock adapter connected to a vacuum pump. Inside, a cylinder acting as a frame supports the surface to be studied, orienting it towards the solid.

Patent application filed out (22/02/2022), application number: P202230143 (Ref. Number: ES1641.1728).

Title: Device for vacuum sublimation.

Owner entity: Consejo Superior de Investigaciones Científicas (CSIC).

Readers are welcomed to check the different advertises that CSIC and ICMAB-CSIC have created regarding the capabilities/uses/novelty of this sublimation system.

https://industry.icmab.es/images/vacuum-sublimation-v.pdf